Computational modeling and analysis of intracardiac flows in simple models of the left ventricle

X. Zheng [a,b], J.H. Seo [a], V. Vedula [a], T. Abraham [b,c], R. Mittal [a,b,*]

[a] *Department of Mechanical Engineering, Johns Hopkins University, Latrobe Hall, 3400 N. Charles Street, Baltimore, MD 21218, USA*
[b] *The Institute for Computational Medicine, Johns Hopkins University, Hackerman Hall, 3400 N. Charles Street, Baltimore, MD 21218, USA*
[c] *Johns Hopkins University Hospital, 601 N. Caroline Street, Baltimore, MD, 21287, USA*

ARTICLE INFO

ABSTRACT

Computational modeling is used to study intracardiac flows in normal and diseased left-ventricles. The left-ventricle is modeled as a semi-prolate-spheroid, and the wall motion is driven by a prescribed ventricular volume-change that consists of five stages: early (E) filling, diastasis, atrial (A) filling, isovolumetric contraction (ISVC) and systole. Simulations are carried out with a parallelized immersed-boundary flow solver that allows us to simulate this flow on a stationary Cartesian grid. The ventricular flow behavior is analyzed to reveal blood flow patterns during both filling and ejection for normal ventricles, as well as ventricles with diastolic and systolic dysfunctions. Impaired relaxation associated with early-stage diastolic dysfunction is modeled by a reduced E/A ratio, and the systolic dysfunction addressed here is obstructive hypertrophic cardiomyopathy (HOCM), where the thickened ventricular septum in the basal region obstructs the outflow tract. Simulations are also performed to study the effect of septal myectomy on the ventricular flow. We examine the characteristic features of these various conditions including vortex dynamics, 'virtual' color M-mode cardiography as well as mixing and transport of blood through the left-ventricle during the entire cardiac cycle.

© 2012 Elsevier Masson SAS. All rights reserved.

1. Introduction

Despite many decades of research, the dynamics of blood flow inside the human heart remains poorly understood. While recent advances in MRI and ultrasound-based (ECHO) imaging techniques have significantly expanded our ability to obtain blood-flow information *in-vivo*, the level of detail available from computational fluid dynamics (CFD) models remains unmatched. However, features of cardiac flows which include highly complex three-dimensional geometries, large-scale boundary motion induced by active (muscle contraction) as well as passive (flow-induced such as in valve leaflets) mechanisms, represent a significant challenge for the computational modeling of cardiac hemodynamics.

The earliest computational modeling of cardiac flows can be traced back to Peskin who developed the immersed boundary method to study the flow patterns inside a whole-heart model, [1,2]. In this method, the flow was solved on a fixed Cartesian grid and the cardiac wall represented by a set of elastic fibers which were immersed in a Cartesian grid. These fibers moved with local flow velocities and the effect of these fibers was transmitted through a smooth delta-function to the fluid. Since the fluid mesh in this method is not required to be body-conformal, it avoids complex mesh generation and remeshing, and is therefore well-suited for flows with immersed elastic boundaries. The smearing of the boundary does, however, reduce the accuracy of surface quantities such as pressure and shear stresses, [3]. This method has been applied to study whole-heart cardiac flow, [4,5] and left-ventricle (LV) flows, [6].

Another approach to modeling cardiac flow combines CFD and CT/MRI/ECHO imaging techniques, [7–10] and has been enabled by advances in medical imaging. In this method, a realistic geometry of the heart and the endocardial motion is extracted from high-resolution medical images and the CFD simulation is driven by the specified endocardial motion. This approach does not require modeling of the cardiac electromechanics and it also has the potential for significantly enhancing the prognosticative value of imaging. However, accurate and rapid segmentation and registration of images for CFD modeling is very challenging and consequently, the application of this approach to cardiac mechanics has been limited to-date, [9,10].

An approach more conducive to fundamental analysis of cardiac flows is one that employs a simplified geometric model of the heart in conjunction with a specified endocardial motion. Many

groups, [11–13] have employed such an approach to study the flow-dynamics of filling (diastole) in the left ventricle. In these studies, the left ventricle is typically represented by a simple shape (such as a semi-prolate-spheroid) and the endocardial kinematics are specified to match the volume flow-rate into the ventricle from the mitral annulus. The evolution of an asymmetric vortex ring as well as vortex-wall interactions have been analyzed and the effect of three-dimensionality, inlet velocity profile and the Strouhal number on the vortex formation and flow patterns have been investigated [11]. Such models have also been employed to study the effect of pathologies such as dilated cardiomyopathy, [14] and myocardial infarction, [15] on the vortex dynamics of filling.

Most studies to-date have, however, employed simple time-varying volume-change profiles to model and examine the dynamics of ventricular filling, [11,12,14,15]. Intercardiac flow effects,i.e. interaction between filling and ejection have, however, not been investigated in detail. Also not studied in detail is the role of multiphasic filling which consists of early (E) filling, diastasis, and atrial (A) filling. In the current study we used computational modeling to examine intercardiac flows in normal as well as diseased left ventricles with realistic volume-change profiles during the entire cardiac cycle. In addition to a normal ventricle, we examine intercardiac flows in left ventricles for two different pathologies: early-stage diastolic dysfunction as characterized by a reduced E/A ratio, [16] and obstructive hypertrophic cardiomyopathy (HOCM), [17]. HOCM is one of the most common inherited heart conditions which manifests through a thickening of the ventricular septum and a dynamic outflow tract obstruction. These features can have a strong influence on the systolic performance of the LV, and in severe cases, can lead to sudden cardiac death. The intercardiac flow pattern, and the transport and mixing of blood in the ventricle are quantified in a number of ways including swirl strength, 'virtual' color M-Mode echocardiography and Lagrangian particle tracking.

In addition to exploring the fundamental aspects of ventricular flows, computational flow modeling has a role to play in the diagnosis and surgical management of heart conditions. We demonstrate the potential of using CFD for surgical planning by modeling the effect of septal myectomy [18] on intercardiac flows for a LV with HOCM. Septal myectomy involves a resection of the hypertrophic mass, but there are no tools available to guide the surgeon in determining the extent and shape of the excision so as to maximize the effectiveness of the surgery. In the current paper, we demonstrate proof-of-concept for surgical modeling by simulating the effect of septal myectomy on the ventricular flow for one configuration of excision.

It is useful at this stage to also point out the potential caveats in the current modeling study. Firstly, the geometric model and wall motion employed for the LV is highly simplified and this simplification will likely affect the LV hemodynamics produced in the simulations. However, past studies [15,11–15,4,19,20] have shown that by carefully choosing all of the major geometric parameters and filling parameters, even simplified models can produce a reasonable representation of real cardiac flow. Secondly, the mitral and aortic valves are excluded from the current study. The mitral valve in particular can have an important effect on the filling flow patterns [21,22]. However, the choice of an appropriate inflow profile coupled with a matching of the vortex formation number can alleviate some of these discrepancies etc. [23]. In the current study, all of the major geometric parameters as well as key flow parameters are chosen to be well within the physiological range. The focus of current study is to use this simplified model to understand fundamental flow features associated with normal as well as diseased hearts. The natural next step in the study would be to include additional anatomical details such as the valve leaflets but it should be noted that that will significantly increase the modeling and computational effort.

2. Numerical method

2.1. Flow model

It is well established that in the large blood vessels, blood acts like a Newtonian fluid. The governing equations for blood flow in the LV are therefore the 3D, unsteady, incompressible Navier–Stokes equations which are

$$\frac{\partial u_i}{\partial x_i} = 0, \qquad \frac{\partial u_i}{\partial t} + \frac{\partial u_i u_j}{\partial x_j} = -\frac{1}{\rho}\frac{\partial p}{\partial x_i} + \nu \frac{\partial^2 u_i}{\partial x_j \partial x_j} \tag{1}$$

where u_i are velocity components in the three directions, p is pressure, and ρ and ν are flow density and kinematic viscosity, respectively. The equations are discretized using a second-order, cell-centered, non-staggered arrangement of the primitive variables u_i and p. A finite-difference method is employed to discretize the equation in space. The advection term is discretized using a second-order Adams–Bashforth scheme and an implicit Crank–Nicolson scheme is employed to discretize the diffusion term and to eliminate the viscous stability constraint. A second-order fractional step method is used to integrate the equation in time. The solution procedure consists of three substeps: in the first step, the solution is advanced by solving the advection–diffusion equation. Subsequent to this, a geometric multi-grid method is used to solve the pressure Poisson equation to obtain the pressure correction. Finally, the velocities are updated using the corrected pressure, [24]. In the version of the fractional-step scheme used here, the face velocity is computed and updated separately from the cell-center velocity. As shown by Zang et al. [25], this separate update of the face-velocity results in discrete mass-conservation to machine accuracy, and leads to a more accurate and robust solution procedure.

The boundary conditions on the immersed boundaries are imposed through a sharp-interface immersed-boundary method (IBM), which is well suited for the simulation of complex moving boundary problems on a Cartesian grid. In this method, a multi-dimensional ghost-cell methodology is used to incorporate the effect of the immersed boundary on the flow. The endocardial surface is represented by an unstructured grid with triangular elements, and this surface is immersed into the Cartesian volume grid. Further details of the immersed boundary flow solver can be found in [24].

3. Simulation setup

A simple model which incorporates many of the key geometrical features of the left-ventricle is employed in the current study. As shown in Fig. 1(a), the endocardial surface of the left ventricle is approximated by a semi-prolate-spheroid and the mitral annulus and aorta are represented by two straight tubes which intersect on the basal (top) surface of the spheroid. The diameter of the mitral orifice is 2.4 cm and the end-systolic lengths of the long and short axes are 8 cm and 4 cm, respectively. These dimensions are carefully chosen to be within or close to the physiological range, [26].

As shown in [27], the endocardial motion of the LV can be decomposed into seven components including an isotropic volume change, twisting, ellipticalization and four asymmetric modes. Compared to the isotropic volume change, the other six components are much smaller and we neglect them in the current study. Thus, the endocardial motion is driven purely by the left ventricular volume change and the ratio of the long and short axes is fixed during the whole cardiac cycle, [27]. The time history of LV volume flow rate during the cardiac cycle is shown in Fig. 1(c). The wave form of this plot is matched to that of [28] and the period of the cardiac cycle is assumed to be 1 s. The end systolic volume
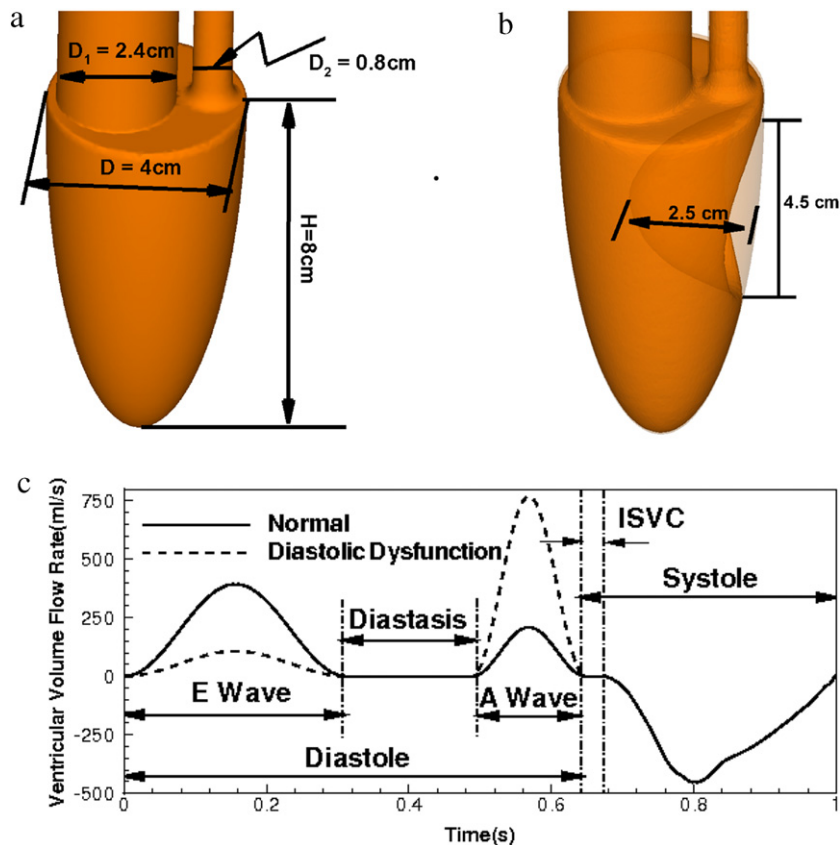
Fig. 1. (a) Geometry of the left ventricle model. (b) Geometry of the left ventricle model with HOCM. (c) Time history of ventricular volume flow rate for normal and abnormal filling during the cardiac cycle.

and end diastolic volume are 67 ml and 147 ml, respectively which are close to the normal physiological values [26]. The resulting stroke volume and ejection fraction are 80 ml and 0.54, which are also within the physiological range, [26]. In the current study, two different types of heart conditions: diastolic dysfunction and obstructive hypertrophic cardiomyopathy (HOCM), are studied and the modeling of these two conditions is described below. In the current study, we define the peak Reynolds number based on peak filling velocity, V_{max}, the mitral orifice diameter D and the kinematic viscosity of blood v as $Re = V_{max}D/v$. For the normal and the impaired relaxation cases, the peak Reynolds number are 745 and 1134 respectively, and these values are in the same range as some other recent studies (e.g. [11]).

3.1. Diastolic heart dysfunction

Diastolic heart dysfunction refers to abnormal ventricular filling that occurs during diastole [16]. During diastole, oxygenated blood enters the LV through the mitral orifice and this filling process is composed of three distinct phases: ventricular relaxation (E-wave), diastasis and atrial contraction (A-wave). The cardiac flow associated with the ventricular filling is highly complex due to the inherent unsteadiness imposed by the large scale active ventricular wall motion, complex vortex formation, and vortex and ventricular wall interaction. In the past, most of the cardiac flow studies have been focused only on the vortical flow during the ventricular relaxation, [11–13]. The effects of the more complex, multiphasic filling process on vortex formation as well as flow transport and mixing remain unclear. Abnormal filling patterns are usually a manifestation of conditions such as diastolic dysfunction [29], myocardial infarction [30] and hypertension [29]. Abnormal filling can also modify the pressure, efficiency and

mixing characteristics of the LV, and lead to a cascade of worsening cardio-pulmonary function [16]. An understanding of the fluid dynamics of abnormal filling associated with diastolic dysfunction could therefore help unravel the components of this cascade.

Diastolic dysfunction is usually manifested through changes in the E/A ratio which is the amplitude of the E and A waves of filling. The physiological range of the E/A ratio for normal filling lies between 1 and 2, whereas that for impaired relaxation associated with early-stage diastolic dysfunction, is less than one [16]. In the current study, the E/A ratios are chosen to be 1.9 [28] for normal filling and 0.14 for impaired relaxation. The ejection-fraction (EF) is usually preserved in the early to mid stages of diastolic dysfunction [16] and we mimic this behavior in our model by keeping the EF same for the two cases. It should be noted that impaired relaxation is associated with a prolonged deceleration of the E-wave but we do not include this effect in our current model. The time history of the volume flow for impaired relaxation associated with diastolic heart dysfunction is shown in Fig. 1(c) as a dashed line.

3.2. Hypertrophic obstructive cardiomyopathy (HOCM)

HOCM is one of the most common inherited cardiac diseases. It manifests itself as a thickened basal ventricular septum and is characterized predominantly by an outflow tract obstruction, [17, 31–33]. While there have been many studies on the pressure gradient in the outflow tract [31,34], the hemodynamics of ejection as well as filling in a LV with HOCM are not well understood. The shape of the hypertrophic mass that we consider here is generally representative of the basal-septal phenotype of HOCM. This obstruction is modeled here as a semi-ellipsoidal bulge [32] located very near to the outflow tract. The maximum protrusion of

Table 1
Comparison of key geometric and flow parameters of the current model with the physiological range.

Parameters	Current value	Physiological value [27,26,11,23]
Ratio of long to short axis	2	2
Diameter of mitral annulus (cm)	2.4	2.0–5.0
LV geometric parameters	2.19	1.7–2.0
End systolic volume (ml)	67	16–143
End diastolic volume (ml)	146	65–240
Stroke volume (ml)	79	55–100
Ejection fraction (%)	54.1	55–70
Cardiac output (L/min)	4.74	4.0–8.0
Heart rate (bpm)	60	60–100
E/A ratio	1.9	1.0–2.0
Vortex formation number	5.7	3.5–5.5
Fraction of SV due to A-wave	0.21	0.2

the mass is about 60% of the base diameter, and it extends over 55% of the height of left ventricle from base to apex thereby presenting a severe obstruction to the outflow tract.

All the geometric parameters in this model have been chosen very carefully to match the physiological range including the long and short axes lengths, long–short axis ration, end diastolic volume, end systolic volume, mean diameter of mitral orifice and LV geometric parameter. The key parameters associated with the ventricular flow are also derived from anatomical data including ejection fraction, E/A ratio, fraction of stroke volume contributed from A-wave filling, vortex formation number, heart rate and cardiac output. The comparison between current values and physiological range are summarized in Table 1. By carefully retaining all of the important geometric parameters of the left ventricle, we expect that we will be able to reproduce the essential features of cardiac flow. The use of this simple model also provides a small, well-defined parametric space that can be explored easily through computational modeling.

The entire model is immersed into a 5.28 cm × 5.28 cm × 16 cm rectangular computational domain. A high resolution 128 × 128 × 256 Cartesian grid is employed in order to resolve the complex flow in the ventricle and a small time-step corresponding to 0.02 ms is employed. Thus, a full cardiac cycle of one second requires 50 000 time-steps. The inlet and outlet flow boundary conditions are only applied on the top of the computational domain. During diastole, a zero velocity boundary condition is applied at the entrance to the aorta to block the aortic passage and the velocity gradient is assumed to be zero at entrance of the atrium which allows the flow to enter the ventricle. During systole, the mitral exit is blocked and all the flow exits through the aorta.

4. Results and discussion

This section summarizes the results from the current computational study.

4.1. Grid-independence study

The grid for the current simulations is chosen after a comprehensive grid refinement study. For this, we considered the normal left ventricle model (Fig. 1(a)) and compare results from simulations on three different $(x \times y \times z)$ grids: 64 × 64 × 128, 128 × 128 × 256 and 256 × 256 × 384. In each simulation, we maintain the same time-step stability constraint by appropriately modifying the time-step while keeping all other parameters to be exactly identical. Results corresponding to this study are shown in Fig. 2(a)–(e). In frames (a)–(c) of Fig. 2, we compare the flow field on the symmetry plane for the three simulations, by plotting the

velocity vectors superposed on top of in-plane vorticity contours. It is clearly evident that except for near wall and corner regions of the coarsest grid, most of the flow features are adequately resolved in all three simulations. We do not notice any significant differences in the flow features between frames (b) and (c) of Fig. 2 indicating that the necessary convergence has been achieved on these grids. To demonstrate grid convergence in a quantifiable manner, we compare the velocity profiles along the axis of the mitral orifice for the three simulations at the end of the E-wave (2(d)) and the end of diastole (2(d)). In either instants, we note only a fairly minor deviation in the profiles and that too for the coarsest grid. The profiles for the two finer grids are virtually indistinguishable. This confirms that the 128 × 128 × 256 grid is sufficient for the current study and all other results presented in this paper are based on this grid.

### 4.2. Intercardiac vortex dynamics: comparison between normal and dysfunctional LVs

Fig. 3(a)–(e) shows the vortex structures for normal filling at five different time instants during the cardiac cycle. During diastole, the vortex formation numbers can be defined as $V/(\pi D^3/4)$, where V is the filling volume and D is the diameter of mitral orifice [23]. For normal filling, the vortex formation numbers are 5.7 and 1.52 for E and A waves respectively. During the flow acceleration associated with the E-wave, a vortex ring is formed at the mitral orifice. At the peak flow rate of the E-wave (shown in Fig. 3(a)), the vortex ring has already pinched off from the mitral orifice and has also become asymmetric due to the eccentric location of the mitral orifice. Similar asymmetric development of the E-wave vortex has also been observed in-vivo [35], in CFD models [36] as well as phase-contrast MRI measurements [9]. In these works, the vortex ring is also found to grow asymmetrically during the diastole and eventually tilt to fill the elongated shape of the ventricle. Furthermore, the direction of the tilting shows a similarity to the MRI [9] measurements in that the left side of the vortex lags behind and the right side moves towards the apex of the ventricle. This tilting of the vortex ring is believed to be essential for the efficient 'flushing' of the whole ventricle.

During the flow deceleration phase of the E-wave, the vortex ring continuously convects towards the apex. Towards the end of the E-wave (Fig. 3(b)) a vortex reconnection occurs between the left side inlet boundary layer vorticity and the leading-edge of vortex in the opposite direction. The inlet boundary starts to develop a vortex ring during this phase but this formation process is not completed. A similar vortex structure has also been reported by Domenichini et al. [11], however, they did not model the subsequent evolution of the vortex structure in their study since the simulation was only conducted for the E-wave. In the current study, the incomplete secondary vortex ring starts to dissipate during diastasis, while the primary vortex ring continuously convects toward apex. In the middle of diastasis (Fig. 3(c)), one side of the primary vortex ring almost reaches the apex while the other side of vortex ring interacts with the septum adjacent to the aortic entrance to form a small ring that surrounds the aorta (Fig. 3(c)). It should be noted that the orientation of these vortex rings are somewhat different from those of [11] and this might be due to the difference in the inlet velocity profiles. The velocity profiles in [11] only have a vertical component whereas our velocity profile at the mitral orifice entrance is a result of the flow development in the mitral pipe and has all components of velocity.

During the flow acceleration phase of the A-wave, the remnants of the two vortex rings from the E-wave have dissipated and a smaller vortex ring is also developed at the mitral orifice. Due to the small vortex formation number of the A-wave, rapid pinch-off
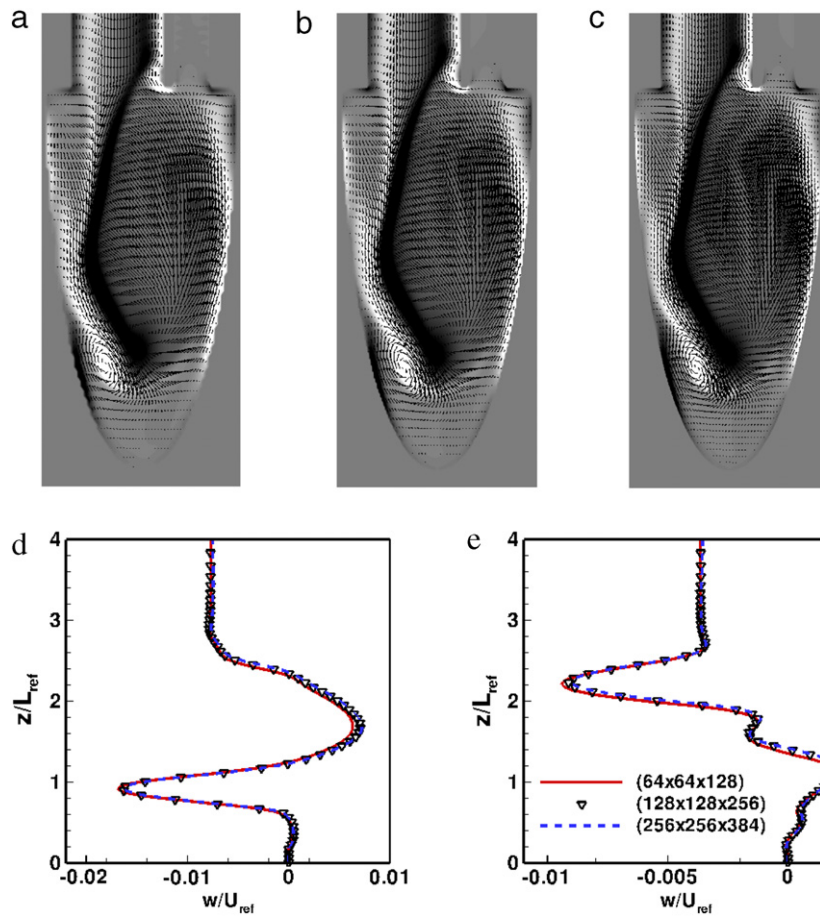
Fig. 2. Grid independence study: (i) vorticity contours and velocity vectors are compared at the end of E-wave ($t = 0.32$ s) on the symmetry plane: (a) Grid-$64 \times 64 \times 128$; (b) Grid-$128 \times 128 \times 256$; (c) Grid-$256 \times 256 \times 384$. (ii) Velocity profile along the mitral axis is compared between various grids: (d) $t = 0.32$ s; (e) $t = 0.66$ s.
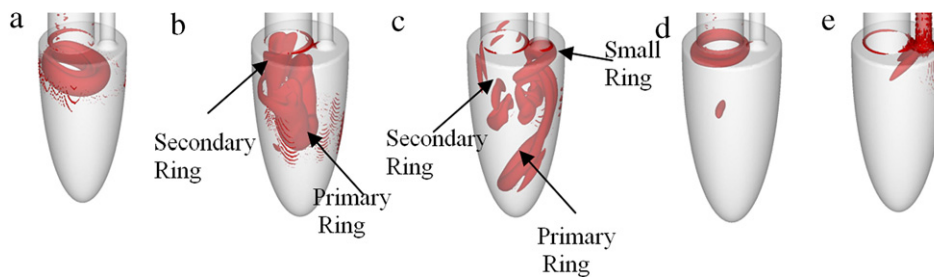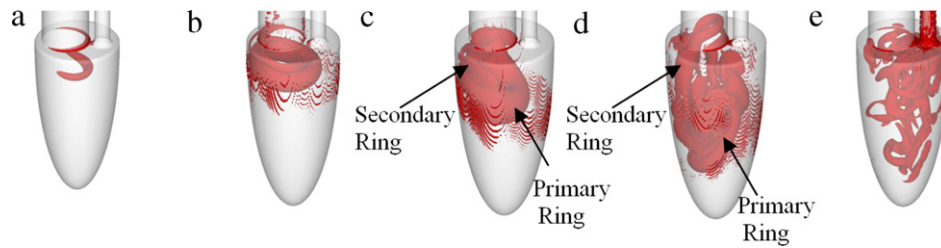

Fig. 3. Vortex structures for normal filling at five different time instants during the cardiac cycle: (a) $t = 0.156$ s; (b) $t = 0.260$ s; (c) $t = 0.400$ s; (d) $t = 0.568$ s; (e) $t = 0.800$ s.

of this vortex is not observed (Fig. 3(d)). Instead, the vortex ring starts to pinch off during the flow deceleration phase and slowly convects towards the apex. At the end of diastole, this vortex ring has not reached the lateral wall and is not fully dissipated. During the systole, the remnants of this vortex ring are pushed into the aorta. (Fig. 3(e)).

For the impaired relaxation case, the vortex formation numbers are 1.52 and 5.7 for the E and A waves respectively, and this case shows a very different vortex topology and evolution as compared to normal filling. Fig. 4(a)–(e) shows the vortex structure at five different time instants for this condition. For this case, more snapshots are chosen during the A-wave which is the dominant phase during filling. During the E-wave, a weaker vortex ring is generated and this asymmetric vortex is still attached to the mitral orifice at the peak flow rate of the E-wave. During the flow deceleration phase of the E-wave, the vortex ring starts to pinch off and convect towards the apex (Fig. 4(a)). This vortex

ring is quickly dissipated during diastasis and has disappeared at the beginning of the A-wave. During the flow acceleration phase of the A-wave, a strong vortex ring is generated and this vortex has already moved away from the mitral orifice (Fig. 4(b)) by the time the A-wave reaches its peak. During the flow deceleration phase of the A-wave, the vortex ring convects towards the apex and the vorticity connection occurs again between the vortex ring and the boundary layer near the mitral orifice (Fig. 4(c)). A secondary incomplete vortex ring is also observed to form at the end of A-wave (Fig. 4(d)). During the iso-volumetric systolic contraction phase, the secondary incomplete vortex interacts with the primary vortex and forms a complex conglomeration of vortex structures around the center of the ventricle. These vortex structures persist during systole, and are finally pushed into the aorta (Fig. 4(e)) during systole.

In the case of the LV with HOCM, the strong vortex ring due to the E-wave interacts with the left endocardium as well as

Fig. 4. Vortex structures for impaired relaxation at five time instants during the cardiac cycle: (a) $t = 0.308$ s; (b) $t = 0.568$ s; (c) $t = 0.600$ s; (d) $t = 0.644$ s; (e) $t = 0.800$ s.
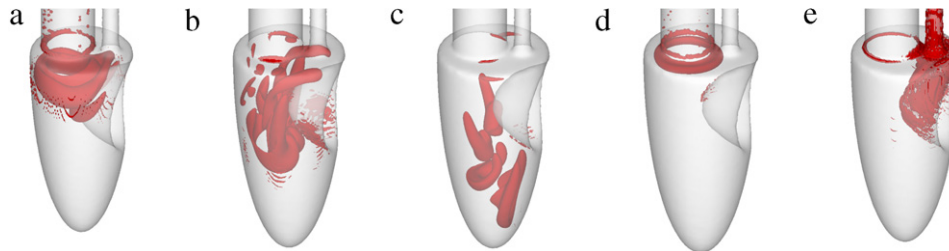

Fig. 5. Vortex structures inside the left ventricle with HOCM at five time instants during the whole cardiac cycle: (a) $t = 0.156$ s; (b) $t = 0.260$ s; (c) $t = 0.400$ s; (d) $t = 0.568$ s; (e) $t = 0.800$ s.

the thickened hypertrophied mass on the right immediately after pinch-off from the base, (Fig. 5(a)). However, in the normal case the interaction with the wall was present only on the left side of the ventricle (Fig. 3(a)) while a shear layer was formed on the right side of the vortex ring. This leads to an asymmetric entrance of the vortex ring into the left ventricle, a feature that is now significantly diminished due to the presence of HOCM. Thus, the vortex ring loses coherence and gets disrupted without filling up the ventricular cavity (Fig. 5(b)). Eventually, all these vortices are rapidly dissipated and only discrete eddies are found scattered near the apex of the left ventricle during diastasis (Fig. 5(c)). Moreover, unlike for the normal left ventricle, these disrupted vortical structures are not effectively redirected back to the aorta due to the obstruction imposed by the bulged septum. Similarly, even during the A-wave, the obstruction due to HOCM prevents the tilting of this vortex ring (see Fig. 5(d)) which is now found to reorient itself along the long axis. However, in both the normal and HOCM cases, the weaker A-wave vortex ring dissipates rapidly without reaching the apex and has a negligible influence on the systolic flow pattern, (Fig. 5(d)). During systole, the presence of hypertrophy leads to the generation of several small scale eddies near the hypertrophied mass (Fig. 5(e)) while ejection is much smoother in the normal case. Thus, HOCM prevents asymmetric filling of the LV and also results in a more complex flow in the outflow tract.

4.3. CFD based color M-mode Doppler echocardiogram

In clinical practice, color M-mode Doppler echocardiogram is often used to estimate the flow propagation velocity in the LV [16]. In contrast to the maximum filling velocities, the flow propagation velocity is insensitive to the preload and as such, is widely used in the clinical practice to assess diastolic dysfunction [37]. In the current study, a 'virtual' color M-mode Doppler echocardiogram along the long axis is constructed from the CFD data. The objective of doing this is two-fold: first this data could eventually be used to validate the simulations against in-vivo measurement and second, this representation of CFD might be more suitable for analysis by clinical practitioners.

The contours of the vertical component of flow velocity along the long axis are used to represent the M-mode and these are plotted in the time-spatial coordinate(shown in Fig. 6). For
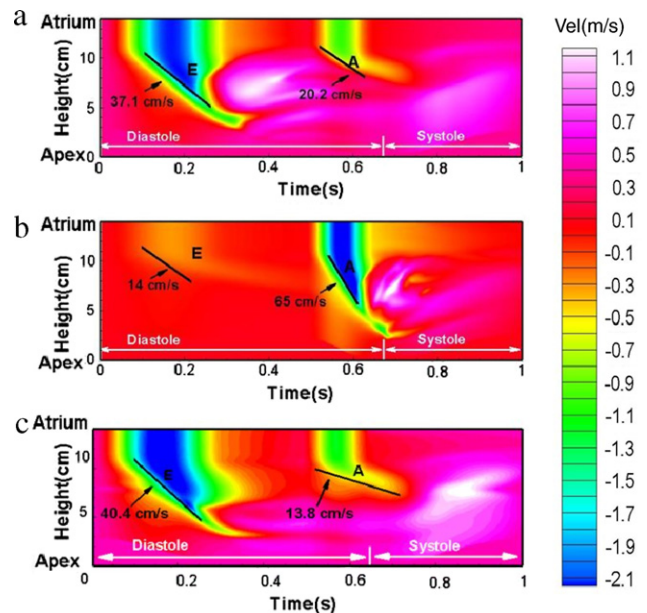

Fig. 6. 'Virtual' color-M mode analysis of propagation velocity via contours of flow velocity along the long-axis: (a) normal filling; (b) impaired relaxation; (c) HOCM. (For interpretation of the references to colour in this figure legend, the reader is referred to the web version of this article.)

normal filling the flow propagation velocity is estimated to be 37.1 cm/s and 20.2 cm/s for the E and A-waves, respectively. The physiological range of flow propagation velocity for the E-wave is 37 ± 13 cm/s [37] and the value from the simulation is therefore well inside the physiological range. For the impaired relaxation case modeled here, the flow propagation velocities are 14 cm/s and 65 cm/s for the E- A-waves respectively. While for the HOCM case, these values were determined to be 40.4 cm/s and 13.8 cm/s, respectively.

4.4. Analysis of blood mixing using Lagrangian particle tracking

The mixing of freshly oxygenated blood from the left atrium and the residual blood in the left ventricle (from the previous cycle)
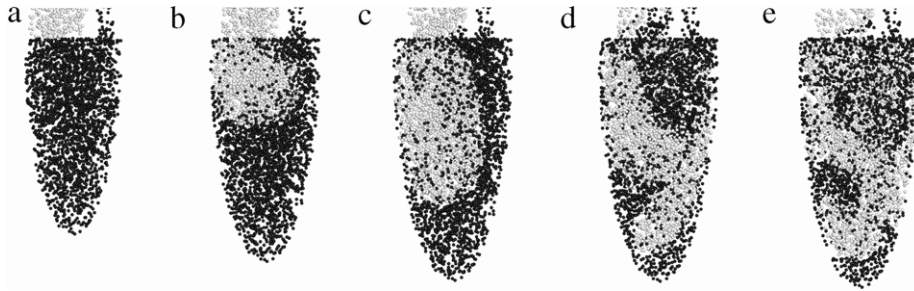
Fig. 7. Distribution of atrial (white) and ventricular (black) blood cells for the normal filling case at five time instants (a) $t = 0.0$ s; (b) $t = 0.156$ s; (c) $t = 0.260$ s; (d) $t = 0.400$ s; (e) $t = 0.568$ s.
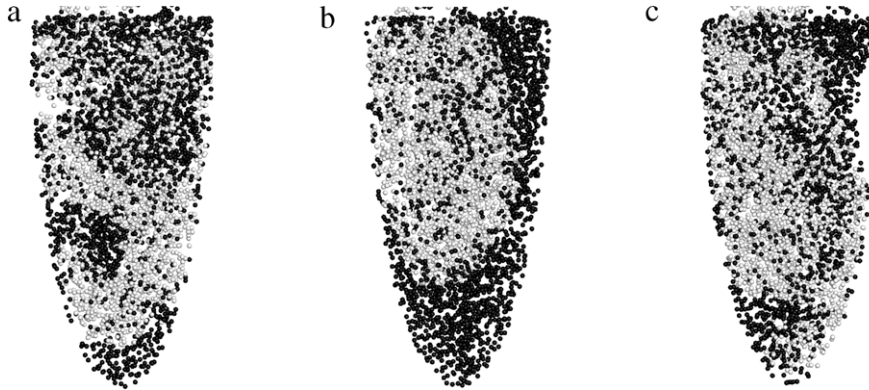

Fig. 8. Distribution of atrial (white) and ventricular (black) blood cells at the end of diastole ($t = 0.644$ s): (a) normal filling; (b) impaired relaxation; (c) HOCM.

depends on intraventricular flow dynamics. The degree of mixing as well as the patterns of atrial and ventricular blood at the time of ejection are important since they determine the residence-time of blood constituents (red-blood cells in particular). In the current section, we analyze the effect of intraventricular flow and vortex dynamics on the blood mixing using a Lagrangian particle tracking approach. At the beginning of diastole, a total of 6000 particles, which represent blood cells, are distributed randomly inside the ventricle, mitral inlet and aorta. The blood cells which are coming through mitral inlet into the ventricle during diastole are tagged as 'atrial' blood cell and the blood cells residing in the ventricle at the beginning of diastole are tagged as 'ventricular' blood cells. The motion of blood cells is tracked by the equation;

$$\vec{x}_p(t + \Delta t) = \vec{x}_p(t) + \int_t^{t+\Delta t} \vec{V}(\vec{x}_p) dt \qquad (2)$$

where $\vec{x}_p$ is the particle position vector and $\vec{V}(\vec{x})$ is the Eulerian velocity vector field obtained from the full Navier–Stokes computation. The time integration is performed by a four-stage Runge–Kutta method and the time-step size used is $\Delta t = 5 \times 10^{-5}$ s. The accuracy of particle tracking has been assessed by re-computing the particle tracking with $\Delta t = 1 \times 10^{-4}$ s. The two results are almost identical with a root-mean squared-difference in the particle positions at $t = 0.644$ s (end diastole) of only 4.5 μm, which is comparable to the size of an actual red blood cell (6–8 μm). Fig. 7 shows the distribution of atrial and ventricular blood cells at different time instants for the normal filling case. As mentioned above, the mixing of the two blood-cell groups is driven by the vortical flow and most of mixing occurs between time $t = 0.260$ (Fig. 7(c)) and $t = 0.400$ (Fig. 7(d)) where strong primary and secondary vortex ring are formed (see Fig. 3). The blood cell particle tracking has also been performed for the impaired relaxation and HOCM cases, and the distributions of atrial and ventricle blood cells at the end of diastole are shown in Fig. 8.
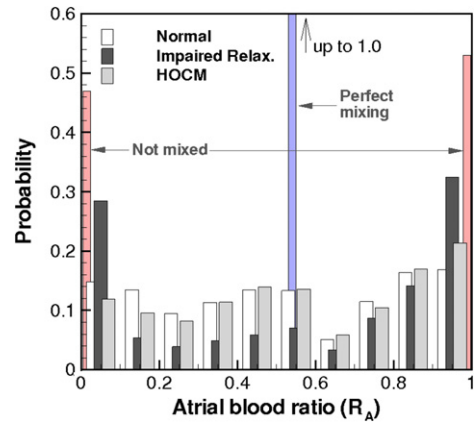
Fig. 9. Probability mass functions of atrial blood ratio (R_A) for normal, impaired relaxation, and HOCM cases.

In order to quantify the degree of mixing for each case, we have evaluated the probability mass function (pmf) of the atrial blood (termed as atrial blood ratio) inside the left ventricle by volume sampling the two particle groups. About 2700, 5 mm³ sampling-volumes are designated in the whole ventricle. Sampling-volumes are allowed to overlap by 50% and each sampling-volume contains at least five particles. For each sampling-volume, the atrial blood ratio (R_A) is computed by $R_A = N_A/N_T$, where N_T is the total number of blood cells inside the sample and N_A is the number of atrial blood cells. In order to increase the reliability of the probability mass function, we have taken an ensemble-average of the probability mass functions for five independent initial particle distributions. We have also repeated the computation with a total of 10 000 particles for the normal filing case, but the maximum difference in the probability from the 6000-particles result is only about 0.15% of the nominal value.
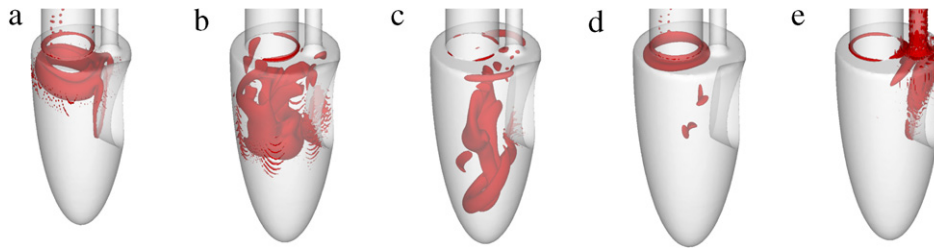
Fig. 10. Vortex structures inside the left ventricle for the HOCM case with 'virtual' septal myectomy at five time instants during the cardiac cycle: (a) $t = 0.156$ s; (b) $t = 0.260$ s; (c) $t = 0.400$ s; (d) $t = 0.568$ s; (e) $t = 0.800$ s.

The probability mass functions computed for the atrial blood ratio are shown in Fig. 9 for normal, impaired relaxation, and HOCM cases. If the atrial and the ventricular blood cells are perfectly mixed, the probability mass function will show a single peak at $R_A = $ EF (Ejection Fraction $= 0.541$), while if the two blood cell groups are not mixed at all, two peaks will appear at 0 and 1. As one can see in Fig. 9, the impaired relaxation case shows a clearly bimodal distribution with noticeably high peaks at low and high value of R_A indicating that the two blood-cell groups are not mixed well for this case. This can also be confirmed qualitatively in Fig. 8. For impaired relaxation, most of atrial blood comes in with the A-wave which occurs just before end-diastole, and thus, there might not be enough time for the mixing to occur. The probability mass function of atrial blood ratio for the HOCM case is very similar to the normal filling case, and most of the noticeable difference is limited to region with $R_A < 0.2$ and $R_A > 0.8$.

4.5. Effect of sepal myectomy on intercardiac hemodynamics

Severe cases of HOCM are usually treated by a procedure called septal myectomy [17,31–33] where the surgeon resects the hypertrophied mass. The objective of this procedure is to remove as much a tissue as needed to recover near-normal outflow tract flow and pressure behavior while at the same time avoiding septal muscle defects or heart blockage due to excess tissue removal, [32]. This exercise in surgical optimization relies primarily on the experience level of the surgeon, since no quantitative tools are available that could predict the effect of surgery on the flow dynamics. However, the current computational modeling approach, enables us to explore various resection options related to this procedure. This kind of modeling approach could potentially be applied to patient-specific surgical management of HOCM in the future but significant challenges in the generation of computational models from imaging data and rapid simulation need to be overcome before this becomes a reality.

Here, we model one case of septal myectomy where a flat portion at the top of the hypertrophied mass is removed in a direction parallel to the long axis of the ventricle. The volume of tissue removed constitutes 16% of the total hypertrophic mass and the filling and ejection vortex dynamics of this case are shown in Fig. 10. A primary vortex ring similar to that of normal LV is formed and it pinches off from the base leaving behind a trailing jet during early filling (E-wave). Additionally, secondary vortices are formed due to the flow interaction with the resected septal wall, (Fig. 10(a)). However, the primary vortex ring still retains the tilt and structure similar to that of the normal case during early filling and convects downstream towards the apex, (Fig. 10(b)). However, unlike the HOCM case, some vortex structures are found to be redirected towards the aorta after reaching the apex, (Fig. 10(c)). The dynamics for this case is found to be very similar to the normal LV during the atrial contraction, with the formation of a weak vortex ring that maintains its structure and orientation similar to that of the normal LV, (Fig. 10(d)). Vortex structures near the outflow tract also correlate well with those of the

normal left ventricle during ejection, (Fig. 10(e)). Thus, even this highly simplified model indicates that near-normal intercardiac flow patterns can be recovered by a relatively small (by volume) resection of the hypertrophied mass. To our knowledge, this attempt at a hemodynamical analysis of septal myectomy is the first of its kind, and a rigorous analysis pertaining to this study will be the motivating factor for future work.

5. Summary

Three-dimensional numerical simulations have been conducted to investigate the vortex dynamics of filling and ejection for normal left ventricles as well as ventricles with diastolic and systolic dysfunctions. Simulations have been subjected to a thorough grid-refinement study to establish the adequacy of the grid used. The simulations employ a realistic multi-phasic ventricular-volume-change profiles during the entire cardiac cycle. In addition to a normal ventricle, we examine intercardiac flows in left ventricles for two different pathologies: early-stage diastolic dysfunction as characterized by a reduced E/A ratio, [16] and obstructive hypertrophic cardiomyopathy (HOCM), [17]. For the normal ventricle, the vortex dynamics of filling is dominated by a tilted vortex ring which is similar to those observed in past studies [35,36,9]. Our simulation of impaired relaxation shows that these conditions lead to complex vortex structures during the A-wave, which persist beyond diastole and affect the ventricular flow during systole. The presence of a large basal-septal obstruction in HOCM is found to disrupt the filling vortex ring and also interfere with the redirection of the flow into the aorta. Lagrangian particle tracking is used to examine diastolic mixing of atrial and ventricular blood for all the above conditions. It is found that while the presence of HOCM has relatively little effect on this mixing, impaired relaxation leads to a reduced level of mixing. Finally, we simulate a case with HOCM where we mimic the effect of septal myectomy, a surgical procedure that involves a resection of the hypertrophic mass. The simulations indicate that even a small resection can potentially result in the resumption of near-normal intercardiac flow.

References

[1] C. Peskin, Flow patterns around heart valves: a digital computer method for solving the equations of motion., Ph.D. Thesis Albert Einstein Coll. Med., Univ. Microfilms 378, 1972 pp. 72–30.
[2] C. Peskin, D.M. McQueen, A three-dimensional computational method for blood flow in the heart I. Immersed elastic fibers in a viscous incompressible fluid, J. Comput. Phys. 39 (1989) 372–405.

[3] Z. Li, M.C. Lai, The immersed interface method for the Navier–Stokes equations with singular forces, J. Comput. Phys. 171 (2) (2001) 822–842.

[4] J.D. Lemmon, A.P. Yoganathan, Three-dimensional computational model of left heart diastolic function with fluid–structure interaction, J. Biomech. Eng. 122 (2000) 109–117.

[5] J.D. Lemmon, A.P. Yoganathan, Computational modeling of left heart diastolic function: examination of ventricular dysfunction, J. Biomech. Eng. 122 (2000) 297–303.

[6] D. McQueen, C. Peskin, Heart Simulation by an Immersed Boundary Method with Formal Second-Order Accuracy and Reduced Numerical Viscosity, third ed., Kluwer Academic Publishers, Boston, 2000.

[7] N.R. Saber, A.D. Gosman, N.B. Wood, P.J. Kilner, C.L. Charrier, D.N. Firmin, Computational flow modeling of the left ventricle based on in vivo MRI data: initial experience, Ann. Biomed. Eng. 29 (2001) 275–283.

[8] N.R. Saber, N.B. Wood, A.D. Gosman, R.D. Merrifield, G. Yang, C.L. Charrier, P.D. Gatahouse, D.N. Firmin, Progess towards patient-specific computational flow modeling of the left heart via combination of magnetic resonance imaging with computational fluid dynamics, Ann. Biomed. Eng. 31 (2003) 42–52.

[9] T. Schenkel, M. Malve, M. Markl, B. Jung, H. Oertel, MRI-based cfd analysis of flow in a human left ventricle methodology and application to a healthy heart, Ann. Biomed. Eng. 37 (3) (2009) 505–515.

[10] V. Mihalef, R. Ionasec, P. Shuarma, B. Georgescu, I. Voigt, M. Suehling, D. Comaniciu, Patient-specific modelling of whole heart anatomy, dynamics and hemodynamics from four-dimensional cardiac CT images, J. R. Soc. Interface Focus 1 (2011) 286–296.

[11] F. Domenichini, G. Pedrizzetti, B. Baccani, Three-dimensional filling flow into a model left ventricle, J. Fluid Mech. 539 (2005) 179–198.

[12] M. Nakanura, S. Wada, T. Mikami, A. Kitabatake, T. Karino, Computational study on the evolution of an intraventricular vortical flow during early diastole for the interpretation of color M-mode doppler echocardiograms, Biomech. Model. Mechanobiol. 2 (2003) 59–72.

[13] M.W.J.G. Georgiadis, A. Pasipoularides, Computational fluid dynamics of left ventricular ejection, Ann. Biomed. Eng. 20 (1992) 81–97.

[14] B. Baccani, F. Domenichini, G. Pedrizzetti, G. Tonti, Fluid dynamics of the left ventricular filling in dilated cardiomyopathy, J. Biomech. 35 (2002) 665–671.

[15] F. Domenichini, G. Pedrizzetti, Intraventricular vortex flow changes in the infarcted left ventricle: numerical results in an idealised 3D shape, Comput. Meth. Biomech. Biomed. Eng. 14 (1) (2011) 95–101.

[16] O.A. Smiseth, M. Tendera, Diastolic Heart Failure, Springer, London, 2008.

[17] B. Maron, Hypertrophic cardiomyopathy: a systematic review, J. Am. Med. Assoc. 287 (10) (2002) 1308–1320.

[18] P. Spirito, C.E. Seidman, W.J. Mckenna, B.J. Maron, Management of hypertrophic cardiomyopathy, N. Engl. J. Med. 30 (1997) 775–785.

[19] T. Talor, H. Okino, T. Yamaguchi, Three dimensional analysis of left ventricular ejection using computational fluid dynamics, J. Biomech. Eng. 116 (1994) 127–130.

[20] H. Watanabe, S. Sugiura, H. Kafuku, T. Hisada, Multiphysics simulation of left ventricle filling dynamics using fluid–structure interaction finite element method, BioPhys. J. 87 (2004) 2074–2085.

[21] O. Pierrakos, P.P. Vlachos, The effect of vortex formation on left ventricular filling and mitral valve efficiency, J. Biomed. Eng. 128 (2006) 527–539.

[22] A. Yoganathan, Z. He, S.C. Jones, Fluid mechanics of heart valves, Annu. Rev. Biomed. Eng. 6 (2004) 331–362.

[23] M. Gharib, E. Rambod, A. Kheradvar, D.J. Sahn, J.O. Dabiri, Optimal vortex formation as an index of cardiac health, PNAS 103 (16) (2006) 6305–6308.

[24] R. Mittal, H. Dong, M. Bozkuittas, F.M. Najiar, A. Vargas, A. Loebbecke, A versatile sharp interface immersed boundary method for incompressible flows with complex boundaries, J. Comput. Phys. 227 (10) (2008) 4825–4852.

[25] Y. Zang, R. Street, J. Koseff, A non-staggered fraction step method for time-dependent incompressible Navier–Stokes equations in curvilinear coordinates, J. Comput. Phys. 114 (1994) 18–33.

[26] J.D. Bronzino, The Biomedical Engineering Handbook, second ed., CRC Press, Boca, Raton, 1999.

[27] T. Arts, W.C. Hunter, A. Douglas, A.M.M. Muijtjens, R.S. Reneman, Description of the deformation of the left ventricle by a kinematic model, J. Biomech. 25 (10) (1992) 1119–1127.

[28] F. Domenichini, G. Querzoli, A.G. Genedese, G. Pedrizzetti, Combined experimental and numerical analysis of the flow structure into the left ventricle, J. Biomech. 40 (2007) 1988–1994.

[29] L. Mandinov, F.R. Eberli, C. Seiler, O.M. Hess, Review: diastolic heart failure, Cardiovasc. Res. 45 (2000) 813–825.

[30] J. Garcia-Rubira, F. Molano, A. Espina, R. Calvo, M. Gonzalez-Valday, J.T. Garcia-Martinez, J.M. Cruz, Abnormal filling pattern of the left ventricle and outcome in acute myocardial infarction., Int. J. Cardiol. 61 (1997) 143–149.

[31] B.J. Maron, M.S. Maron, E.D. Wigle, E. Braunwald, The 50-year history, controversy, and clinical implication of left ventricular outflow tract obstruction in hypertrophic cardiomyopathy, J. Am. Coll. Cardiol. 54 (3) (2009) 191–200.

[32] M.V. Sherrid, Pathophysiology and treatment of hypertrophic cardiomyopathy, Prog. Cardiovasc. Dis. 49 (2) (2006) 123–151.

[33] S.R. Ommen, P.M. Shah, A.J. Tajik, Left ventricular outflow tract obstruction in hypertrophic cardiomyopathy: past, present and future, Heart 94 (2008) 1276–1281.

[34] M.V. Sherrid, O.W. Pinzon, A. Shah, F.A. Chaudhry, Reflections of inflection in hypertrophic cardiomyopathy, J. Am. Coll. Cardiol. 54 (3) (2009) 212–219.

[35] P.J. Kilner, G. Yang, A.J. Wilkes, R.H. Mohiaddin, N. Firmin, M.H. Ycoub, Asymmetric redirection of flow through the heart, Nature Lett. 404 (2000) 759–761.

[36] T. Doenst, K. Spiegel, M. Reik, M. Markl, J. Henning, S. Nitzsche, F. Beyersdorf, H. Oertel, Fluid-dynamics modeling of the human left ventricle: methodology and application to surgical ventricular reconstruction, Ann. Thorac. Surg. 87 (2009) 1187–1195.

[37] J.M. Carcia, N.G. Smedira, N.L. Greenberg, M. Main, M.S. Firstenberg, J. Odabashian, J.D. Thomas, Color M-mode doppler flow propagation velocity is a preload insensitive index of left ventricular relaxation: animal and human validation, J. Am. Coll. Cardiol. 35 (2000) 201–208.